A VLT study of metal-rich extragalactic H II regions. I. Observations and empirical abundances

Fabio Bresolin, Daniel Schaerer, Rosa M. González Delgado, Grazyna Stasinska

A&A 441, 981–997 (2005)
DOI: 10.1051/0004-6361:20053369

Astronomy & Astrophysics

A VLT study of metal-rich extragalactic H II regions

I. Observations and empirical abundances⋆,⋆⋆

F. Bresolin[1], D. Schaerer[2,3], R. M. González Delgado[4], and G. Stasińska[5]

[1] Institute for Astronomy, University of Hawaii, 2680 Woodlawn Drive, Honolulu 96822, USA
e-mail: bresolin@ifa.hawaii.edu
[2] Observatoire de Genève, 51 Ch. des Maillettes, 1290 Sauverny, Switzerland
e-mail: daniel.schaerer@obs.unige.ch
[3] Laboratoire Astrophysique de Toulouse-Tarbes (UMR 5572), Observatoire Midi-Pyrénées, 14 avenue E. Belin, 31400 Toulouse, France
[4] Instituto de Astrofísica de Andalucía (CSIC), Apdo. 3004, 18080 Granada, Spain
e-mail: rosa@iaa.es
[5] LUTH, Observatoire de Paris-Meudon, 5 place Jules Janssen, 92195 Meudon, France
e-mail: grazyna.stasinska@obspm.fr

Received 5 May 2005 / Accepted 3 June 2005

ABSTRACT

We have obtained spectroscopic observations from 3600 Å to 9200 Å with FORS at the Very Large Telescope for approximately 70 H II regions located in the spiral galaxies NGC 1232, NGC 1365, NGC 2903, NGC 2997 and NGC 5236. These data are part of a project to measure the chemical abundances and characterize the massive stellar content of metal-rich extragalactic H II regions. In this paper we describe our dataset, and present emission line fluxes for the whole sample. In 32 H II regions we measure at least one of the following auroral lines: [S II] λ4072, [N II] λ5755, [S III] λ6312 and [O II] λ7325. From these we derive electron temperatures, as well as oxygen, nitrogen and sulphur abundances, using classical empirical methods (both so-called "T_e-based methods" and "strong line methods"). Under the assumption that the temperature does not introduce severe biases, we find that the most metal-rich nebulae with detected auroral lines are found at $12 + \log(\mathrm{O/H}) \simeq 8.9$, i.e. about 60% larger than the adopted solar value. However, classical abundance determinations in metal-rich H II regions may be severely biased and must be tested with realistic photoionization models. The spectroscopic observations presented in this paper will serve as a homogeneous and high-quality database for such purposes.

Key words. galaxies: abundances – galaxies: ISM – galaxies: stellar content

1. Introduction

While the analysis of the emission-line spectra of extragalactic H II regions has been essential in the past three decades to investigate the abundance of heavy elements in star-forming galaxies, we still lack the observational and theoretical information to adequately understand the metal-rich end (roughly solar and above) of the nebular abundance scale. This situation is explained by the inherent difficulty of measuring abundances in this regime, however it also affects the study of the inner portions of virtually all spiral galaxies, as a consequence of their radial abundance gradients (e.g. Vila-Costas & Edmunds 1992; Zaritsky et al. 1994).

The key observational element at low abundance is the strength of the [O III] λ4363 auroral line, which allows, in combination with the nebular [O III] $\lambda\lambda$4959,5007 lines, to measure the electron temperature T_e of the gas, upon which the line emissivities strongly depend. It is well known that, as the cooling efficiency of the gas increases with the oxygen abundance, the [O III] auroral line becomes too faint to be observed with the largest telescopes even at modest metallicity. In this case nebular abundance studies generally rely on *statistical methods*, based on the measurement of strong nebular lines only. The use of $R_{23} = ([\mathrm{O\,II}]\,\lambda3727 + [\mathrm{O\,III}]\,\lambda\lambda4959,5007)/\mathrm{H}\beta$ (Pagel et al. 1979) has become widespread in this context, however several different semi-empirical calibrations for this index have been proposed at high abundance (Edmunds & Pagel 1984; Dopita & Evans 1986; McGaugh 1991; Pilyugin 2001, and

⋆ Based on observations collected at the European Southern Observatory, Chile, proposal ESO 71.B-0236.
⋆⋆ Tables 5–9 are only available in electronic form at the CDS via anonymous ftp to
cdsarc.u-strasbg.fr (130.79.128.5) or via
http://cdsweb.u-strasbg.fr/cgi-bin/qcat?J/A+A/441/981

others). Additional abundance indicators, which rely on emission lines present in the optical spectra of H II regions other than those from oxygen, in particular sulphur and nitrogen, have also appeared in the literature (Alloin et al. 1979; Díaz & Pérez-Montero 2000; Denicoló et al. 2002; Pettini & Pagel 2004). The usefulness of the statistical methods goes beyond the derivation of abundance gradients in spirals (Pilyugin et al. 2004), as these methods can be used in chemical abundance studies of a variety of objects, including low surface brightness galaxies (de Naray et al. 2004) and star-forming galaxies at intermediate and high redshift, where around-solar oxygen abundances have been found (Kobulnicky & Kewley 2004; Shapley et al. 2004).

Recently, starting with the works by Castellanos et al. (2002) and Kennicutt et al. (2003), and especially with the use of large-aperture telescopes of the 8 m-class by Pindao et al. (2002), Garnett et al. (2004a) and Bresolin et al. (2004), it has become possible to measure auroral lines, such as [N II] λ5755, [S III] λ6312 and [O II] λ7325, at high oxygen abundance [up to $12 + \log(\mathrm{O/H}) \simeq 8.9$]. This extends the application of the *direct method* (T_e-based) of abundance determination to the high-metallicity regime, therefore by-passing the need to use R_{23} or similar indicators to derive the metallicity in the inner regions of spirals, as well as allowing empirical calibrations of the statistical methods at high abundance. These works conclude that the statistical methods appear to overestimate abundances around the solar value by as much as 0.2–0.3 dex (we adopt $12 + \log(\mathrm{O/H})_\odot = 8.69$, following Allende Prieto et al. 2001). There are, however, uncertainties affecting these T_e-based chemical abundances from the temperature stratification of metal-rich H II regions, which can introduce important biases in the measured abundances, as shown by Stasińska (2005).

In order to resolve some of the issues related to metal-rich extragalactic H II regions, we started a project in which the first step is to obtain high-quality spectra of a large sample of these objects. In this paper we present our observations and analyse them with classical, empirical methods. Whenever possible, we derive electron temperatures by using observed auroral lines. We use these temperatures to obtain direct T_e-based abundances for a sizeable sample of H II regions. We compare these abundances with those derived from statistical methods based on strong lines only.

In a future paper we will carry out a detailed chemical analysis, with the aid of photoionization models, of a subset of the sample, in order to verify the importance of abundance biases at high metallicity and provide a reliable calibration for strong line methods.

Another paper of this series will deal with the stellar populations embedded in metal-rich H II regions. It has been suggested by several authors that at high metallicity the massive star Initial Mass Function deviates from the standard Salpeter function, for example with an upper mass cutoff as low as 30 $M_\odot$ (Goldader et al. 1997; Bresolin et al. 1999; Thornley et al. 2000). However, the presence of strong wind signatures in the UV spectra of nuclear starbursts is evidence against the depletion of massive stars in metal-rich environments (González Delgado et al. 2002). Moreover, the detection of Wolf-Rayet (WR) stars in metal-rich H II regions allowed Pindao et al. (2002) to dispute these claims (see also Schaerer et al. 2000 and Bresolin & Kennicutt 2002), and to show that the progenitors of WR stars (revealed in the integrated spectra by their broad emission line features at 4680 Å and 5808 Å) are at least as massive as 60 $M_\odot$.

A high-metallicity environment strongly facilitates the formation of WR stars, through the action of stellar winds driven by radiation scattered in metal lines. As a consequence, the percentage of H II regions expected to display WR features in their spectra varies significantly as a function of metallicity, from 40% at 1/5 solar metallicity to 70–80% at solar metallicity and above (Meynet 1995, Schaerer & Vacca 1998). These theoretical predictions are well supported by recent observations. For example, Crowther et al. (2004) detected WR features in nearly 70% of the ~200 H II regions they surveyed in the metal-rich galaxy M 83, while 6 out of 10 H II regions analyzed spectroscopically in M 51 by Bresolin et al. (2004), although far from representing a complete sample, display strong WR emission. Therefore, investigating metal-rich nebulae, through the properties (flux and equivalent width) of the emission features of the embedded WR stars and the statistics of WR stars relative to the total number of ionizing stars, offers an opportunity to constrain evolutionary models of massive stars.

In this paper we describe new spectroscopic observations obtained at the Very Large Telescope of H II regions in the galaxies NGC 1232, NGC 1365, NGC 2903, NGC 2997 and NGC 5236 (=M 83). We present the main observational data, with tables containing emission line fluxes for about 70 H II regions. This paper is structured as follows: we describe the observations and the data reduction in Sect. 2, and discuss the general properties of the H II regions sample in Sect. 3. Electron temperatures are derived from the available auroral lines in Sect. 4, and we compute direct abundances of oxygen, nitrogen and sulphur in Sect. 5. We summarize our paper in Sect. 6.

2. Observations and data reduction

2.1. Target selection

For this project we selected galaxies where the available nebular studies from the literature indicated the presence of high-abundance H II regions (Pagel et al. 1979; McCall et al. 1985; Vila-Costas & Edmunds 1992; Zaritsky et al. 1994; Roy & Walsh 1997; van Zee et al. 1998; Bresolin & Kennicutt 2002). In most cases, this judgement has been based on the strength of the oxygen emission lines, through the use of the semi-empirical abundance indicator R_{23} and its calibration from different authors (Edmunds & Pagel 1984; Dopita & Evans 1986; Kobulnicky et al. 1999; Pilyugin 2001). Only in the case of NGC 1232 was a *direct* measurement of above-solar oxygen abundance in one H II region available, from the detection of the [N II] λ5755 and [S III] λ6312 auroral lines by Castellanos et al. (2002). A brief compilation of galactic parameters of our sample is given in Table 1.

The H II regions for the spectroscopic work were selected by examining narrow-band Hα images from various sources. Given the nature of the multi-object spectroscopy technique

Table 1. Galaxy parameters.

Galaxy	RA (2000)[a]	Dec (2000)[a]	Morphological[a] type	Distance[b] (Mpc)	i[c] (deg)	PA[c] (deg)	R_{25}[c] (arcsec)
NGC 1232	$03^h\ 09^m\ 45\overset{s}{.}5$	$-20°\ 34'\ 46''$	SAB(rs)c	19.6	29	108	222
NGC 1365	$03^h\ 33^m\ 36\overset{s}{.}4$	$-36°\ 08'\ 25''$	SBb(s)b	17.2	57	32	337
NGC 2903	$09^h\ 32^m\ 10\overset{s}{.}1$	$+21°\ 30'\ 03''$	SB(s)d	9.4	61	17	378
NGC 2997	$09^h\ 45^m\ 38\overset{s}{.}8$	$-31°\ 11'\ 28''$	SA(s)c	9.4	41	110	300
NGC 5236	$13^h\ 37^m\ 00\overset{s}{.}9$	$-29°\ 51'\ 57''$	SAB(s)c	4.5	27	45	395

[a] Source: NASA/IPAC Extragalactic Database.
[b] NGC 1232, NGC 2903, NGC 2997: Lyon/Meudon Extragalactic Database; NGC 1365: Freedman et al. (2001); NGC 5236: Thim et al. (2003).
[c] Source: RC3.

Table 2. Observing log and sky conditions.

Galaxy	Observing date	Sky conditions	Seeing (arcsec)			Exposure time (s)		
			600B	600R	300I	600B	600R	300I
NGC 1232	Aug. 5 2003	photometric	0.6–0.8	0.6–0.8	0.6–0.8	1660	3060	1340
NGC 1365	Sep. 19 2003	clear	1.1–1.3	0.9–1.1	1.2–1.5	2000	2600	1600
NGC 2903	Apr. 24 2003	clear	0.9–1.0	1.5–1.8	1.1–1.2	800	1320	680
NGC 2997	May 3,5 2003	clear, cirrus	1.0–1.2	1.0–1.2	1.1–1.2	2000	2600	1600
NGC 5236	Apr. 23 2003	clear	0.8–0.9	0.9–1.0	0.7–0.8	650	1190	560

adopted for our observations and the presence of radial abundance gradients in the target galaxies, we have included in our sample nebulae with different luminosities and chemical abundances, with those in the central galactic regions likely to approach or exceed the solar oxygen abundance. When possible, the brightest H II regions at a given projected galactocentric distance were chosen, in order to increase the odds of detecting faint auroral lines and WR stellar features in emission. *R*-band images obtained at the VLT prior to the spectroscopic observations were used to measure H II region positions and to define the multi-object spectroscopy setups, via the FIMS software provided by the European Southern Observatory's User Support Group.

2.2. Observations

The spectra were obtained in service mode at the VLT with the FORS2 spectrograph, in the period March to September, 2003. Seeing conditions were typically better than 1.2 arcsec, as summarized in Table 2. Each galaxy was observed with one setup composed of up to 19 slitlets, each 1 arcsec wide and 20 arcsec long, distributed over the $6\overset{'}{.}8 \times 6\overset{'}{.}8$ FORS field of view. The complete optical and near-infrared spectra of the H II regions were obtained with three different grisms: 600B (~3500–5200 Å, 5 Å *FWHM*), 600R (~5000–8500 Å, 6 Å *FWHM*) and 300I (~6500–10 000 Å, 11 Å *FWHM*). This choice of grisms ensured that the auroral and stellar features in the blue/red part of the spectrum, when detected, were observed with sufficient spectral resolution for the analysis, while still covering the near-infrared wavelengths, necessary for measuring the [S III] λ9069 lines. Different total exposure times (divided into two contiguous exposures) were used for the 5 galaxies, as summarized in Table 2.

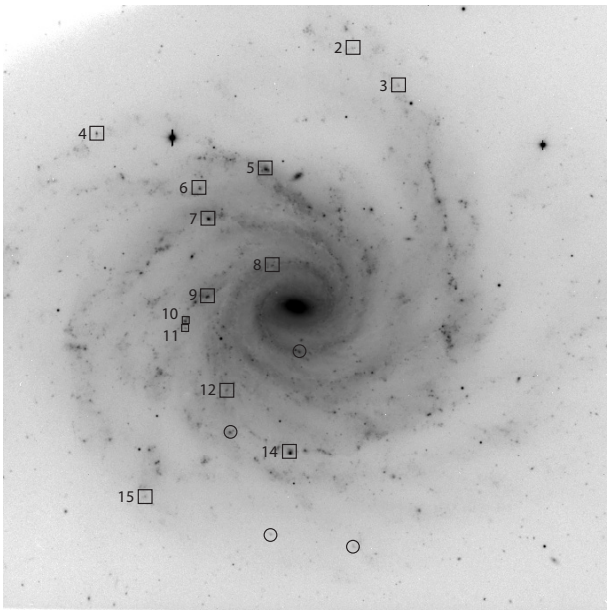

Fig. 1. H II region identification for NGC 1232. In this and in the following charts, derived from *R*-band FORS1 or FORS2 images, the slitlet numbers for the objects marked by squares correspond to those in Tables 3 and 4. The open circles mark additional objects observed spectroscopically, but not included in the analysis of this paper, because of the extreme faintness or the absence of emission lines. Orientation is North to the top and East to the left.

Finding charts for the observed H II regions can be found in Figs. 1–5, where we have marked with squares the nebulae analyzed in this paper, and with circles some additional targets not included in the analysis, due to the low signal-to-noise of their spectra, or the heavy contamination by underlying stellar components. One of these excluded objects is a quasar at redshift $z \simeq 2.55$ (see Appendix A).

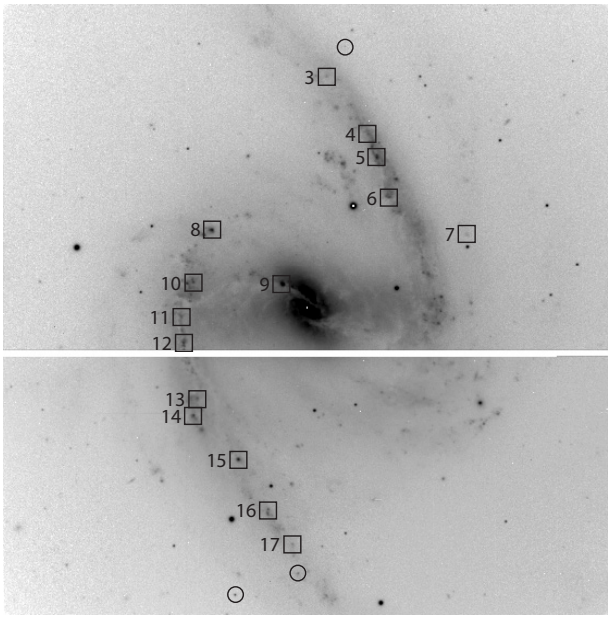

Fig. 2. H II region identification for NGC 1365. The gap in the FORS2 CCD mosaic runs horizontally.

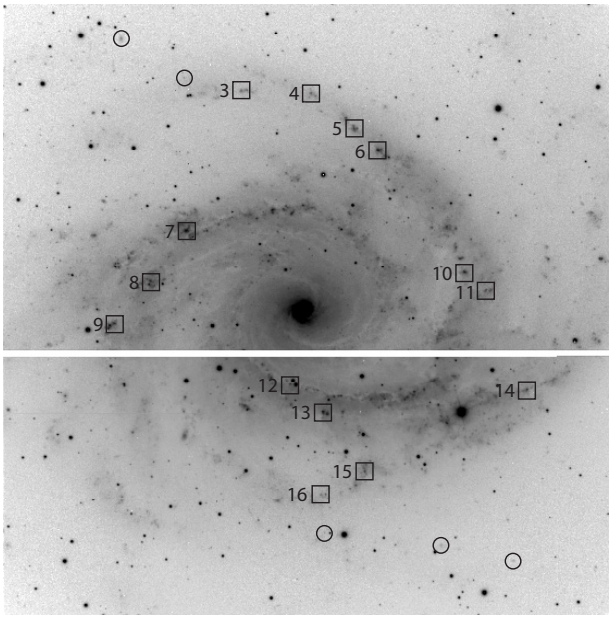

Fig. 4. H II region identification for NGC 2997. The gap in the FORS2 CCD mosaic runs horizontally.

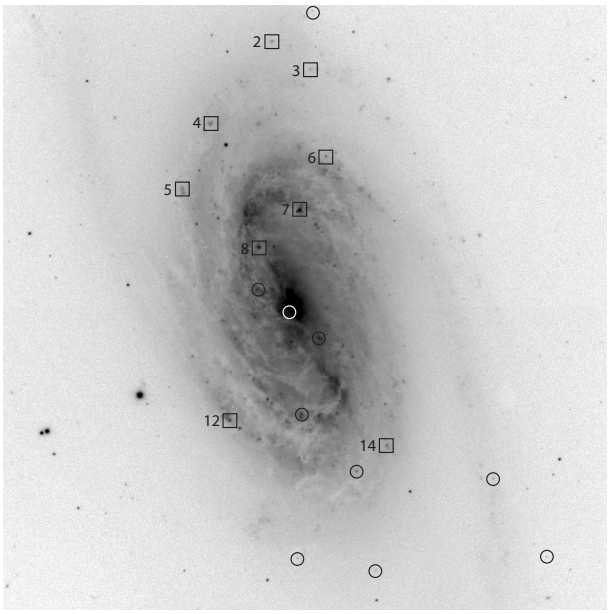

Fig. 3. H II region identification for NGC 2903.

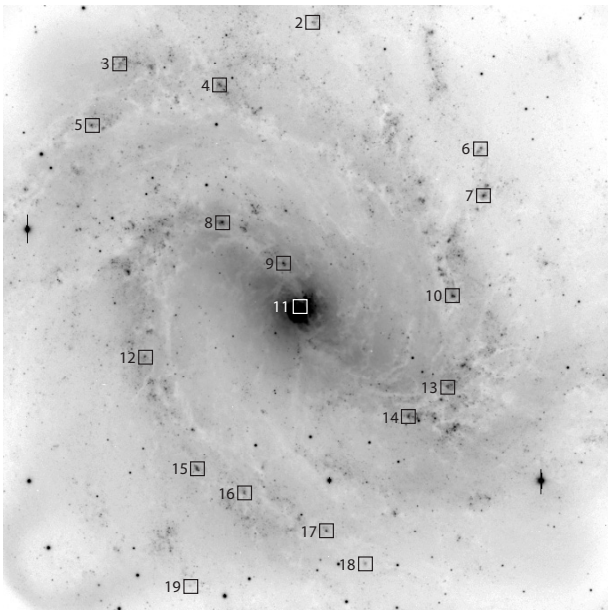

Fig. 5. H II region identification for NGC 5236.

2.3. Data reduction

The data reduction was carried out using standard IRAF[1] routines, and included bias and flat field corrections, wavelength and flux calibrations, and atmospheric extinction correction. The flux calibration provided by the observed standard star spectra appears satisfactory for the whole wavelength range, except at the longest wavelengths, above roughly 9200 Å. The three spectral segments were then flux-normalized using lines in common: He I λ5876 between 600B and 600R, H α+[N II] $\lambda\lambda$6548,6583 and [S II] $\lambda\lambda$6716,6731 between 600R and 300I. Only in rare instances did this procedure introduce corrections larger than 10% relative to the scaling provided by the independent flux calibrations. In those 14 cases where the He I λ5876 was not included in both the 600B and the 600R spectra, the flux scaling factor was obtained by requiring that Hα/Hβ = 2.86, as in case B at T_e = 10 000 K, after the proper extinction correction, determined from Hβ and higher-order Balmer lines, had been applied.

For the interstellar extinction correction we used the Balmer decrement measured by the Hα, Hγ and Hδ lines, and the reddening law of Seaton (1979), as parameterized by

[1] IRAF is distributed by the National Optical Astronomy Observatories, which are operated by the Association of Universities for Research in Astronomy, Inc., under cooperative agreement with the National Science Foundation.

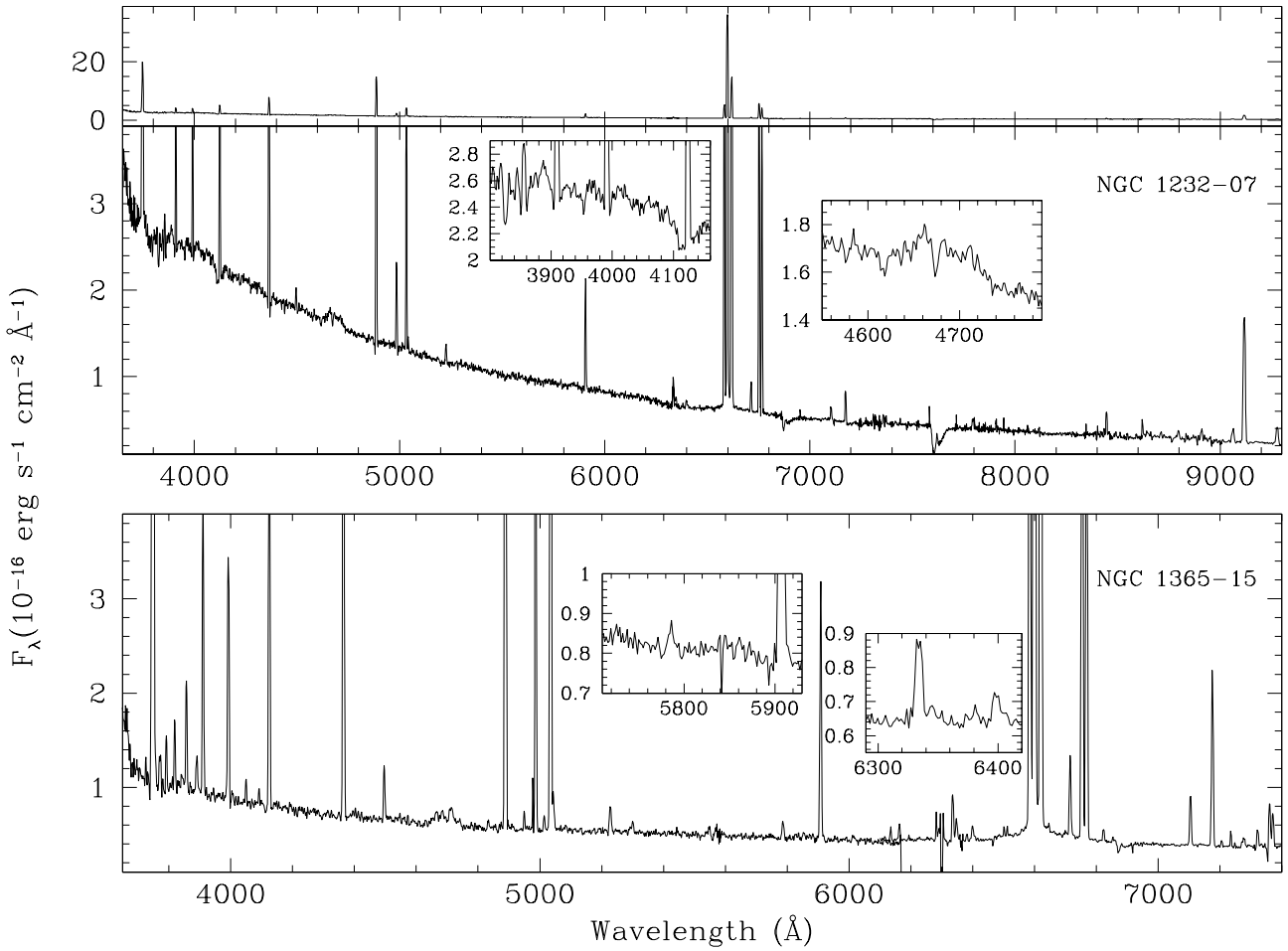

Fig. 6. (*Top*) The combined spectrum of NGC 1232-07, showing the full extent of the spectral coverage of our observations. Two different vertical scales are used. The insets show zoomed-in portions of the spectrum, where strong stellar features are located: Balmer absorption lines and WR emission lines. (*Bottom*) Portion of the spectrum observed in NGC 1365-15, with the auroral lines [N II] λ5777 and [S III] λ6312 highlighted.

Howarth (1983), assuming a total-to-selective extinction ratio $R_V = A_V/E_{B-V} = 3.1$, and case B theoretical ratios at 10 000 K (Hummer & Storey 1987). We iteratively solved for the value of c(Hβ) and for the absorption originating from the underlying stellar population, assuming that the equivalent width of the absorption component is unchanged throughout the Balmer series. The value for the latter was found to be in the range 0–5 Å. In several cases the Hα/Hβ and the Hδ/Hβ gave consistent results, but differing from the extinction measured from Hγ/Hβ. A weighted average for c(Hβ) was then adopted. We also experimented with the reddening law of Cardelli et al. (1989), and found it even more difficult to converge on a value for c(Hβ) using a single value for the absorption equivalent width, although the estimated extinction was, in general, in fair agreement with that measured with the Seaton law.

We display in Figs. 6 and 7 a few examples of H II region spectra extracted from our sample. The spectrum in the top panel of Fig. 6 (NGC 1232-07) shows the complete wavelength range covered by the combination of the 600B, 600R and 300I grisms. Zoomed-in examples of stellar features in the blue, namely absorption components and the WR emission bump, are also included. The bottom panel shows the blue-red spectral range in NGC 1365-15, where auroral lines are easily detected: the insets show the [N II] λ5755 and [S III] λ6312 lines. The top panel of Fig. 7 shows part of the spectrum of NGC 2903-08, a low-excitation object (notice the weak [O III] $\lambda\lambda$4959,5007 lines) where WR features are seen at 4686 Å, 5696 Å and 5808 Å. The bottom panel displays the specrum of NGC 5236-11, a bright hot-spot H II region in the nucleus of the galaxy. The WR blue bump, first detected by Bresolin & Kennicutt (2002, their object A), is quite strong. Stellar and interstellar absorption features are seen throughout this spectrum.

2.4. Line fluxes: results

In Tables 3 and 4 we present for each H II region in the five target galaxies the following quantities: slit number (the original slit in the FORS2 multi-object spectroscopy setup), the offsets from the galaxy center (in arcsec, measured increasing to the East and North), the deprojected galactocentric radius (calculated from the observed position and the galactic parameters of Table 1), the size of the spectral extraction window (in arcsec), the extinction c(Hβ), the equivalent width of the

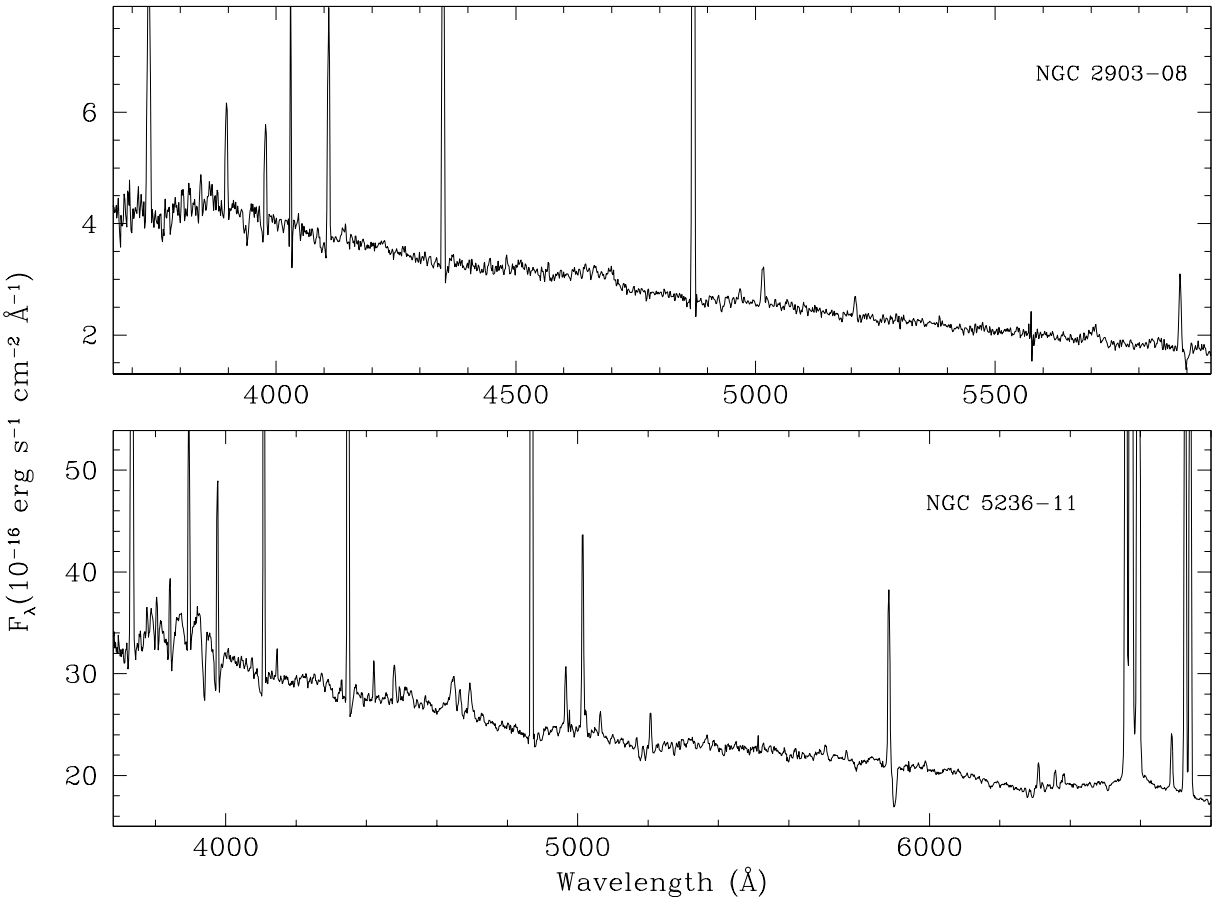

Fig. 7. (*Top*) The blue portion of the spectrum of NGC 2903-08, a low-excitation H II region, as indicated by the weak [O III] $\lambda\lambda$4959, 5007 emission. Emission features due to WR stars are seen at 4680 Å (WN subtypes), 5696 Å and 5808 Å (WC subtypes). (*Bottom*) Portion of the spectrum of NGC 5236-11, a hot-spot H II region located in the nucleus of the galaxy. Several stellar (WR 4680 bump, Balmer absorption lines) and interstellar (Ca II, Na I) features are seen, together with auroral lines ([N II] λ5755, [S III] λ6312).

nebular Hβ emission and its flux, and the equivalent width of the Balmer line absorption estimated from the extinction correction procedure. As mentioned earlier, we do not include in these two tables those objects which have a S/N ratio that is too low for a useful analysis, and those objects where, despite a high S/N in the continuum, the brightest Balmer emission lines were either absent or almost completely lost in the underlying stellar absorption. This leaves us with a sample of 69 H II regions.

Line flux ratios, relative to Hβ = 100, for nebular emission lines of interest are given in Tables 5–9. The associated errors reflect the uncertainties in the flat field correction and in the flux calibration, as well as the statistical errors. As these tables show, auroral lines ([S II] λ4072, [N II] λ5755, [S III] λ6312, [O II] λ7325), which allow the determination of electron temperatures of the various ions, were measured in 32 H II regions, nearly half of the whole sample. The He I lines have been corrected for an average absorption component, following the recipe given in Kennicutt et al. (2003).

2.5. Line fluxes: comparisons

Several of our target H II regions have been observed by previous investigators, and we carried out a survey of the literature, in order to compare our measurements with the published line fluxes. The quality of the published material is heterogeneous (in terms of sensitivity, detector, telescope aperture, slit size, etc.), but a simple comparison can still be useful, in that it could reveal important systematic effects in the new, deeper observations. We have thus extracted measurements of [O II] λ3727, [O III] λ5007, [N II] λ6583 and [S II] $\lambda\lambda$6716, 6731 from the following papers:

NGC 1232 van Zee et al. (1998);
NGC 1365 Pagel et al. (1979), Alloin et al. (1981), Roy & Walsh (1988), Roy & Walsh (1997);
NGC 2903 McCall et al. (1985), Zaritsky et al. (1994), van Zee et al. (1998);
NGC 2997 Edmunds & Pagel (1984), Walsh & Roy (1989);
NGC 5236 Bresolin & Kennicutt (2002).

The resulting comparison is displayed in Fig. 8, where the reddening-corrected line intensities (in units of Hβ = 100) from this paper and from the literature are plotted along the horizontal axis and the vertical axis, respectively. Symbols with different colors are shown for the different papers used in this comparison. Excluding for a moment the first panel concerning [O II] λ3727, we do not find evidence for systematic

Table 3. H II region global properties: NGC 1232, NGC 1365 and NGC 2903.

Slit number	Offsets[a] *EW*	NS	r_0[b] (arcsec)	Extraction width ($''$)	$c(H\beta)$	Hβ emission *EW* (Å)	Flux[c]	Balmer line absorption *EW* (Å)
				NGC 1232				
02	−38	176	199	2.2	0.16 ± 0.10	140	7.8	0.0
03	−69	150	178	2.2	0.00 ± 0.05	76	4.7	0.0
04	135	118	199	2.1	0.44 ± 0.10	296	40.1	2.0
05	20	93	109	3.9	0.39 ± 0.05	109	90.7	1.0
06	65	80	116	2.7	0.28 ± 0.05	57	25.9	0.6
07	59	60	94	2.0	0.25 ± 0.05	57	78.2	0.3
08	16	28	37	3.3	0.46 ± 0.08	62	12.9	0.0
09	60	7	62	4.9	0.40 ± 0.10	29	23.5	0.0
10	75	−10	76	3.1	0.44 ± 0.10	83	28.0	0.2
11[d]	75	−14	77	1.8	0.44 ± 0.05	176	6.2	0.0
12	47	−57	77	2.7	0.50 ± 0.10	62	9.1	0.0
14	4	−99	111	4.2	0.02 ± 0.05	174	85.2	2.0
15	102	−129	172	3.4	0.07 ± 0.05	180	6.9	2.0
				NGC 1365				
03	−14	162	221	2.0	0.35 ± 0.10	204	14.6	2.5
04	−43	122	202	1.7	0.26 ± 0.05	15	5.3	1.8
05	−49	105	189	4.2	0.40 ± 0.05	48	92.3	0.3
06	−57	77	168	2.3	0.36 ± 0.05	28	16.0	0.5
07	−111	52	224	2.8	0.05 ± 0.05	68	7.5	2.1
08	66	55	95	3.8	0.38 ± 0.05	59	105.4	0.3
09	17	17	25	4.3	0.25 ± 0.10	42	177.9	4.8
10	79	18	119	1.9	0.55 ± 0.10	44	31.2	0.0
11	87	−6	147	1.8	1.06 ± 0.10	13	6.7	0.1
12	86	−24	159	1.1	0.69 ± 0.10	43	25.8	0.0
13	76	−63	180	2.7	0.48 ± 0.15	56	24.4	0.0
14	79	−75	196	3.9	0.61 ± 0.05	50	44.0	0.4
15	48	−105	188	3.7	0.43 ± 0.10	195	109.6	0.0
16	27	−141	207	1.9	0.20 ± 0.05	40	20.8	0.0
17	10	−164	221	1.9	0.03 ± 0.03	98	11.6	1.1
				NGC 2903				
02	14	178	192	4.6	0.05 ± 0.05	31	14.7	0.5
03	−12	159	190	3.4	0.03 ± 0.05	100	16.1	2.9
04	55	123	138	3.1	0.60 ± 0.10	27	13.7	0.2
05	75	78	139	2.9	0.31 ± 0.10	77	51.2	1.2
06	−22	100	137	2.0	0.28 ± 0.06	217	28.5	1.2
07	−5	64	77	4.9	1.04 ± 0.10	28	128.2	0.8
08	23	38	48	2.9	0.39 ± 0.10	43	118.9	2.5
12	43	−78	145	2.4	0.39 ± 0.05	43	66.9	0.2
14	−64	−95	129	2.0	0.49 ± 0.15	1	10.6	0.0

[a] In arcsec, positive to the East and to the North of the galaxy center.
[b] Deprojected galactocentric distance.
[c] Measured flux. In units of 10^{-16} erg s^{-1} cm^{-2} Å^{-1}.
[d] Second object in slitlet 10.

deviations from the dashed lines, representing the locations at which the points would lie in case of a perfect match between our dataset and the published ones. A similar conclusion could be drawn for the [O II] λ3727 line comparison, were it not for a small number of outliers in the top part of the diagram. Among these are our H II regions NGC 2903-14 and NGC 1232-10 (compared to van Zee et al. 1998, which are also discrepant objects in the panel concerning [S II] $\lambda\lambda$6716, 6731),

Table 4. H II region global properties: NGC 2997 and NGC 5236.

Slit	Offsets[a]		r_0[b]	Extraction	$c(H\beta)$	Hβ emission		Balmer line
number	*EW*	NS	(arcsec)	width ($''$)		*EW* (Å)	Flux[c]	absorption *EW* (Å)
					NGC 2997			
03	43	154	212	2.7	0.10 ± 0.10	97	15.3	0.0
04	−6	153	196	4.4	0.27 ± 0.10	121	26.7	0.0
05	−36	128	163	3.9	0.14 ± 0.10	147	54.9	3.7
06	−52	113	146	4.6	0.28 ± 0.05	151	115.3	3.7
07	81	57	122	3.2	0.99 ± 0.10	77	59.6	0.0
08	106	22	119	2.2	1.00 ± 0.10	23	13.5	0.4
09	131	−8	135	5.3	0.27 ± 0.05	34	27.9	0.2
10	−112	28	116	4.2	0.07 ± 0.05	51	38.4	2.1
11	−128	16	131	3.8	0.18 ± 0.04	95	13.9	1.8
12	9	−50	64	1.9	0.76 ± 0.07	42	13.1	1.8
13	−14	−69	93	2.8	0.56 ± 0.05	96	49.5	2.2
14	−156	−54	188	4.3	0.40 ± 0.05	189	27.4	4.5
15	−43	−110	157	3.0	0.67 ± 0.05	51	22.2	2.0
16	−13	−126	166	3.9	0.41 ± 0.00	52	14.0	1.5
					NGC 5236			
02	−13	193	207	1.8	0.58 ± 0.05	23	26.5	0.6
03	117	165	203	1.5	0.53 ± 0.10	102	98.6	0.0
04	50	151	163	2.8	0.35 ± 0.05	26	123.1	1.0
05	136	124	184	2.6	0.70 ± 0.10	45	130.0	0.0
06	−126	108	186	1.5	0.14 ± 0.05	47	76.2	2.0
07	−128	76	166	1.7	0.13 ± 0.10	13	71.0	1.5
08	48	58	75	2.3	0.68 ± 0.08	12	142.0	0.9
09	7	30	32	1.7	1.12 ± 0.10	46	137.8	0.6
10	−107	8	115	2.6	0.29 ± 0.10	27	175.4	1.2
11	−5	−1	5	1.6	0.27 ± 0.05	48	1264.6	2.6
12	100	−33	116	3.1	0.48 ± 0.10	64	167.6	0.5
13	−104	−54	119	2.5	0.34 ± 0.10	55	212.6	1.3
14	−78	−73	107	1.9	0.15 ± 0.08	31	166.1	1.5
15	65	−109	141	1.4	0.22 ± 0.08	7	47.5	1.9
16	33	−125	141	2.2	0.61 ± 0.05	74	148.6	1.3
17	−22	−151	159	2.3	0.36 ± 0.15	35	105.1	0.3
18	−48	−173	185	2.6	0.57 ± 0.10	39	29.8	0.6
19	70	−188	221	2.5	0.60 ± 0.05	32	11.8	0.0

[a] In arcsec, positive to the East and to the North of the galaxy center.
[b] Deprojected galactocentric distance.
[c] Measured flux. In units of 10^{-16} erg s^{-1} cm^{-2} Å^{-1}.

NGC 2997-6 (compared with Edmunds & Pagel 1984), and a number of objects compared with Roy & Walsh (1997). While it is difficult to assess the ultimate reason(s) for these discrepancies, we note that in some cases (e.g. NGC 2903-14, NGC 1232-10) there are ambiguities regarding the centering of the slit, due to multiple, separate bright emission spots. In other cases, there are likely some problems with the previously published fluxes, as for the fiber-fed spectrograph observations of Roy & Walsh (1997), as stated by these authors themselves. Better agreement is, in fact, found with their imaging spectrophotometry of NGC 1365 (Roy & Walsh 1988). Finally, excellent agreement is found with some of the most recent, CCD-based work used in the comparison (Bresolin & Kennicutt 2002; and van Zee et al. 1998, once the two problematic objects mentioned above have been justifiably excluded). Different extinction estimates could explain some of the discrepancies seen

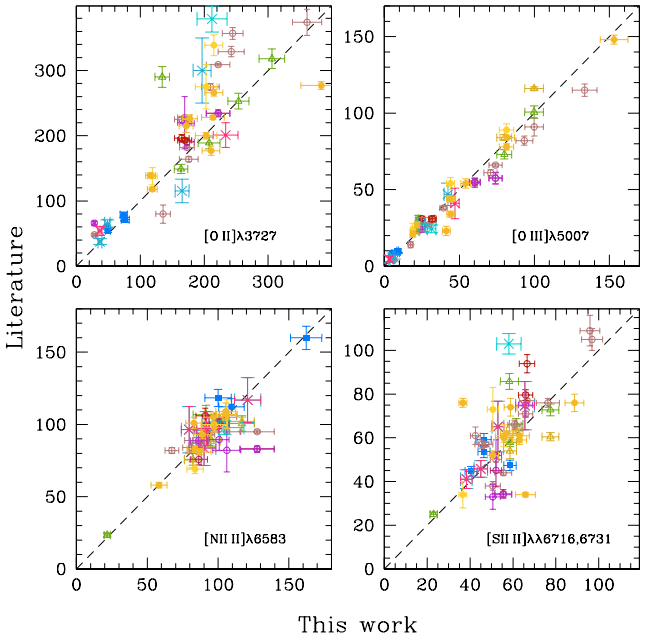

Fig. 8. Comparison of reddening-corrrected line intensities (in units of Hβ = 100) measured in the current work (x-axis) with published values from the literature (y-axis). The four panels refer to the strong lines [O II] λ3727 (*top left*), [O III] λ5007 (*top right*), [N II] λ6583 (*bottom left*) and [S II] $\lambda\lambda$6716,6731 (*bottom right*). The five target galaxies shown are: NGC 1232 (open triangles), NGC 1365 (open circles), NGC 2903 (crosses), NGC 2997 (full circles), NGC 5236 (open squares). Different colors are used for different comparison data, which are taken from the studies mentioned in the text.

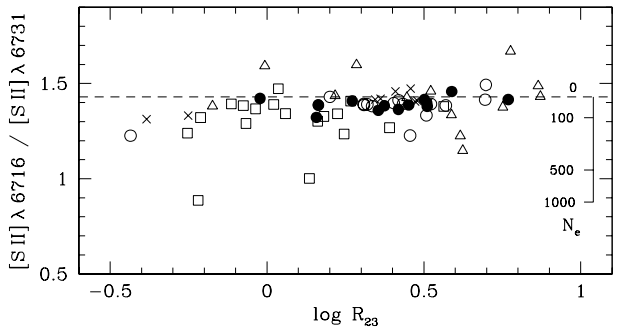

Fig. 9. The electron density-sensitive ratio [S II] λ6716/[S II] λ6731 plotted against the empirical abundance indicator R_{23} for our H II region sample. The scale on the right provides an approximate density scale (in cm^{-3}). The zero-density limit is indicated by the dashed line. Here and in the following diagrams we use the following symbols to differentiate nebulae in the different galaxies: NGC 1232 (*open triangles*), NGC 1365 (*open circles*), NGC 2903 (*crosses*), NGC 2997 (*filled circles*) and NGC 5236 (*open squares*).

in Fig. 8. The tighter agreement seen in the [O III] line flux comparison, relative to the lower-excitation lines, might also be an indication that, at least in some cases, the effects of varying slit aperture, orientation and centering can be significant, since higher ionization is produced in physically smaller nebular volumes, which are more likely to be included even in narrow slits. The effects of differential atmospheric refraction cannot be excluded, either. For our new H II region sample such effects are likely to be negligible, because of the small airmass of the observations (<1.1) or the approximate alignment of the slits along the parallactic angle.

3. Empirical diagrams

3.1. General properties of the nebulae

We can assess some general properties of the H II region sample and the quality of the data by looking at diagrams involving a number of crucial line ratios. In Fig. 9 we show the density-sensitive ratio [S II] λ6716/[S II] λ6731 as a function of the abundance-sensitive indicator R_{23}. The sulphur line ratio reaches a "zero-density limit" at [S II] λ6716/[S II] λ6731=1.43 (T_e = 10 000 K), shown by the dashed line. Almost all of the observed nebulae lie at this limit or just slightly below, with corresponding electron densities up to a few hundred particles cm^{-3} (as shown by the density scale on the right). The highest densities are encountered for two objects in NGC 5236: the central hot-spot H II region #11 ($N_e \simeq$ 1000 cm^{-3}) and the inner-disk H II region #13. The results displayed in this diagram justify the low-density assumption made for the subsequent analysis of the H II region sample.

According to the relative radiative transition probabilities in the O^{2+} and N^+ ions, we expect that the line ratios [O III] λ5007/[O III] λ4959 and [N II] λ6583/[N II] λ6548 be nearly equal to 3. Figure 10 shows that this is indeed the case. The dot-dashed lines show the ±10% deviation from the predicted value. The higher dispersion in the [O III] doublet line ratio can be explained by the fact that these lines are generally fainter than the [N II] lines.

The excitation properties of the H II regions are summarized in the diagrams shown in Fig. 11, where the line ratios [N II] λ6583/Hα and [S II] $\lambda\lambda$6716,6731/Hα, both involving low excitation metal lines, are plotted against [O III] λ5007/Hβ. The H II region sequence is extremely tight in both cases, and comprises objects of mostly low excitation, as expected from the selection of the targets. High-excitation objects (log[O III] λ5007/Hβ > 0) would populate the upper part of the diagram (see similar plots in Bresolin & Kennicutt 2002 and Kennicutt et al. 2000), where the theoretical upper boundaries from Dopita et al. (2000, shown here by full lines) turn sharply to the left.

The nebular extinction c(Hβ) appears to be in the typical range observed in extragalactic H II regions. Its radial distribution within the five galaxies is shown in Fig. 12, using the galactocentric distance normalized to the galactic isophotal radius. There is a slight tendency for larger values of the extinction towards the central regions of the galaxies, at least in the sense that objects with very low c(Hβ) are found only at $R/R_{25} > 0.4$.

3.2. Abundance estimates from statistical methods

Abundance estimates of H II regions can be made by statistical methods based on strong lines and by direct methods based on the measurement of the electron temperature. Until recently, the latter methods could not be applied for metal-rich H II regions, because the lines necessary to derive the

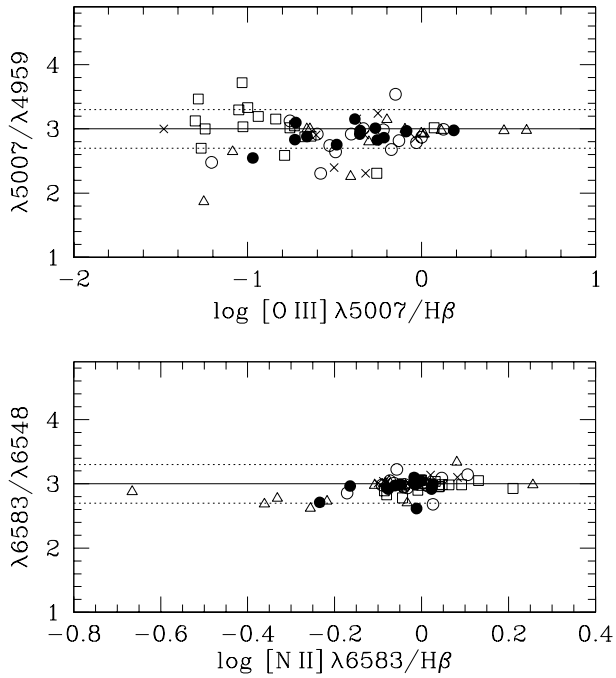

Fig. 10. The ratio between the measured [O III] λ5007 and [O III] λ4959 fluxes (*top*) and between the [N II] λ6583 and [N II] λ6548 fluxes (*bottom*), compared with the theoretical expectation ([O III] λ5007/[O III] λ4959 = [N II] λ6583/[N II] λ6548 = 3), drawn as a continuous line. The dotted lines show the ±10% deviations from the predicted value.

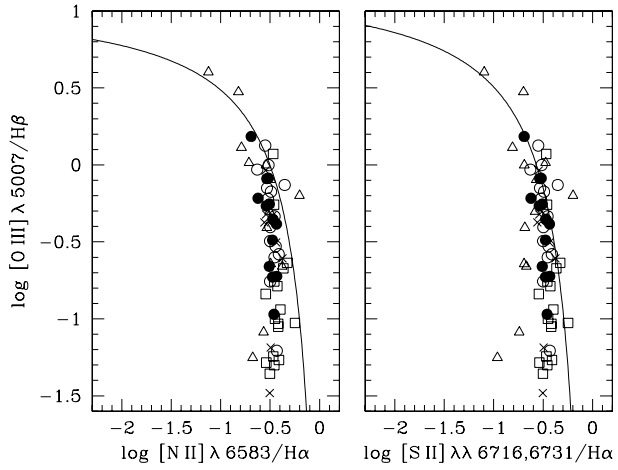

Fig. 11. Nebular diagnostic diagrams showing the excitation sequence of our sample. As a function of log([O III] λ5007/Hβ) we plot log([N II] λ6583/Hα) (*left*) and log([S II] $\lambda\lambda$6716,6731/Hα) (*right*). The curves represent the theoretical upper boundaries calculated by Dopita et al. (2000).

electron temperature were too weak to be measured. There is however a growing amount of data that allow such measurements in regions with very faint auroral lines (Bresolin et al. 2004; Kennicutt et al. 2003; Pindao et al. 2002). Our VLT spectra allow this for a number of objects. In the following, we use our data to derive abundances with the methods described by Bresolin et al. (2004). However, as noted by Stasińska (2005), these methods are likely to produce strong biases in metal-rich

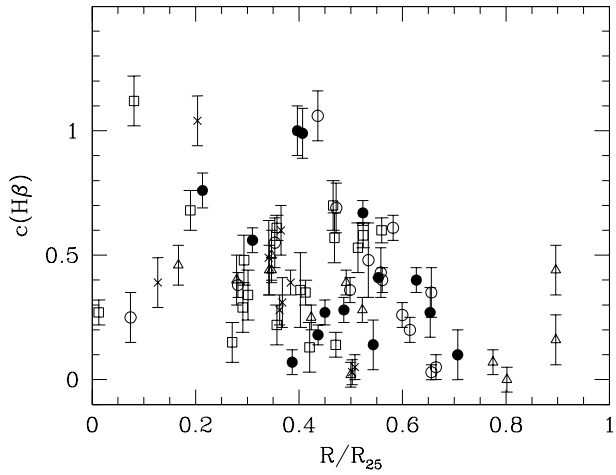

Fig. 12. The radial distribution of the extinction c(Hβ) within the target galaxies. The deprojected radial distances of the individual H II regions have been normalized to the isophotal radius R_{25} of the parent galaxy.

H II regions, and we postpone any strong astrophysical implication of our results to a future paper, where we will discuss in detail the elemental abundances in our set of objects. We first derive abundances using published strong line calibrations, but keeping in mind that such calibrations are extremely uncertain at the high-abundance end.

Out of the different statistical methods found in the literature, we considered the following: R_{23} = ([O II] λ3727 + [O III] $\lambda\lambda$4959, 5007)/Hβ (Pagel et al. 1979), S_{23} = ([S II] $\lambda\lambda$6716, 6731 + [S III] $\lambda\lambda$9069,9532)/Hβ (Díaz & Pérez-Montero 2000), $N2$ = log ([N II] λ6583/Hα) (Denicoló et al. 2002) and O3N2 = log {([O III] λ5007/Hβ)/([N II] λ6583/Hα)} (Alloin et al. 1979; Pettini & Pagel 2004). For S_{23}, since we lacked the sulphur λ9532 line measurements, we estimated the intensity of this line from λ9069 and the theoretical ratio λ9532/ λ9069 = 2.44.

The relationship among these different abundance indicators is shown in Fig. 13, where we have chosen to plot R_{23} against the remaining indicators. The dotted lines provide the values corresponding to the solar abundance, $12 + \log(\mathrm{O/H})_\odot = 8.69$ (Allende Prieto et al. 2001), when using the calibrations of the different indexes from Pettini & Pagel (2004, O3N2 and N2) and Díaz & Pérez-Montero (2000, S_{23}). It should be noted that the latter indicator is, like R_{23}, non-monotonic, so that a decrease of S_{23} below $\log R_{23}$ = 0.3 (roughly corresponding to the solar O/H value, according to the Pilyugin 2001 calibration) corresponds to an increase in the oxygen abundance (see Díaz & Pérez-Montero 2000). Virtually all of the H II regions analyzed here belong to the upper branch of R_{23}, following the condition [N II] λ6583/[O II] λ3727 > 0.1 to define upper-branch objects (van Zee et al. 1998).

The diagrams in Fig. 13 suggest that our H II region sample contains a number of high abundance objects, although the well-known uncertainties in the calibration of the strong line methods, especially at the metal-rich end, prevent us from

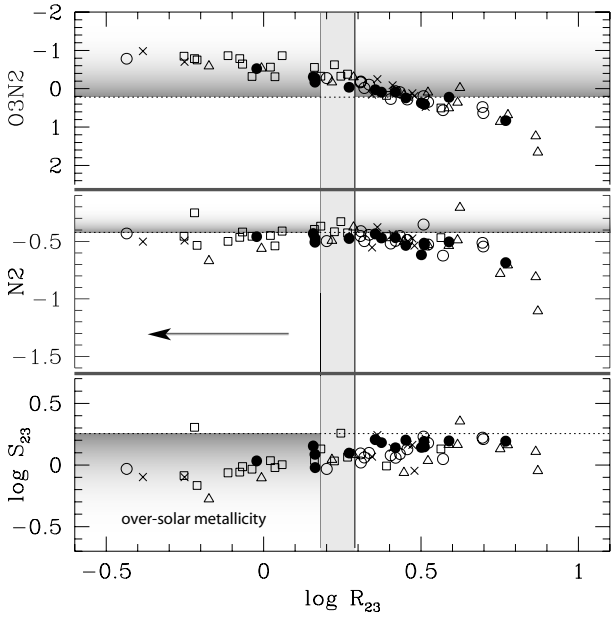

Fig. 13. Comparison of statistical abundance indicators: R_{23} plotted against *O3N2* (*top*), *N*2 (*middle*) and $\log S_{23}$ (*bottom*). The horizontal dotted lines show the index value corresponding to the solar O/H abundance [$12 + \log(\mathrm{O/H})_\odot = 8.69$, Allende Prieto et al. 2001], according to the calibrations of Pettini & Pagel (2004, O3N2, N2) and Díaz & Pérez-Montero (2000, S_{23}). The shaded areas below or above these lines define the regions of over-solar metallicity. The vertical light-grey band represents the solar O/H value derived from the R_{23} calibration of Pilyugin (2001), for the range of the excitation parameter ($P = 0.1$–0.3) which comprises the majority of the H II regions in our sample. The arrow shows the direction of increasing oxygen abundance according to the R_{23} method.

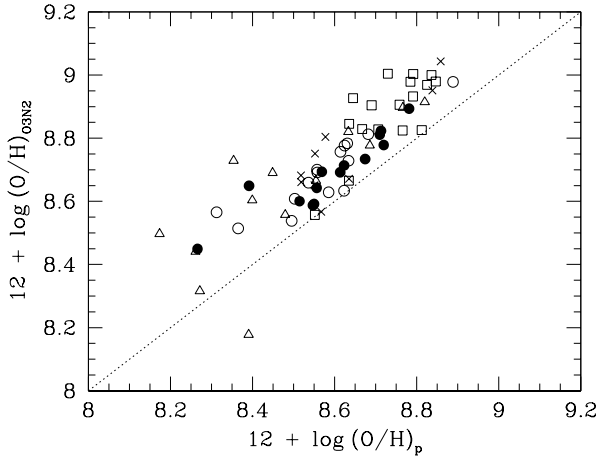

Fig. 14. Oxygen abundance from statistical methods: the *P*-method (Pilyugin 2001) against O3N2 (Pettini & Pagel 2004).

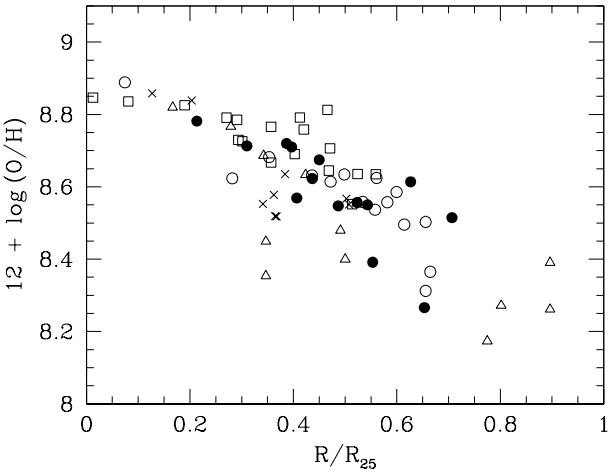

Fig. 15. The radial oxygen abundance gradients in the 5 galaxies, estimated via the *P*-method of Pilyugin (2001). The deprojected radial distances of the H II regions are normalized to the isophotal radius of the parent galaxy.

providing an accurate metallicity scale. For example, both O3N2 and S_{23} would indicate the presence of many H II regions with oxygen abundance well over the solar value, while *N*2 seems to level off at the solar value for the majority of the sample.

In order to quantify the oxygen abundances from empirical methods, we considered the R_{23} indicator, as calibrated by Pilyugin (2001), and O3N2, as calibrated by Pettini & Pagel (2004). In the former case, we adopted the upper branch (high metallicity) version of the calibration, which is applicable when the estimated abundance is $12 + \log(\mathrm{O/H}) > 8.2$ (true for all objects in the sample, except for NGC 1232-15). The comparison between the oxygen abundances obtained from the two indicators is displayed in Fig. 14. An offset of approximately 0.1 dex between the two methods is apparent. According to this diagram, the most metal-rich H II regions in our sample have an abundance of $12 + \log(\mathrm{O/H}) \simeq 8.9$–$9.0$, which is approximately twice the currently accepted solar value. Finally, we display in Fig. 15 the radial oxygen abundance gradients for the target galaxies, as estimated from Pilyugin's *P*-method. Qualitatively these gradients appear quite similar to each other, even though differences in the slopes can be found: note, for example, the somewhat flatter gradient in NGC 5236 (open squares) compared to the remaining galaxies.

4. Auroral lines and electron temperatures

In this section we apply the standard technique of measuring nebular electron temperatures from line ratios involving auroral lines. As seen in Tables 5–9, we have measured one or more of the [O II] λ7325, [N II] λ5755, [S III] λ6312 and [S II] λ4072 lines in several H II regions from our sample. These can be combined with stronger lines to form different line ratios, in short [O II]3727/7325, [N II](6548,6584)/5755, [S III](9069,9532)/6312 and [S II](6716,6731)/4072, which are highly sensitive to the electron temperature. Once the temperature-sensitive emissivities are calculated from T_e, the abundance of the various chemical elements can be derived. At high metallicity, however, the auroral lines do not necessarily provide a good measure of T_e, due to the biases introduced by the presence of temperature gradients within the nebulae (Stasińska 2005). The complications that these effects introduce on the derivation of chemical abundances will be treated in a separate paper. Here we will follow the standard procedure, as if these biases were not present, but with the warning

that the electron temperatures and abundances derived can be erroneous. Ultimately, we will need to verify our direct abundances, as derived here, with detailed nebular models.

Electron temperatures have been obtained from the line ratios listed above using the five-level atom program *nebular* in IRAF/STSDAS v. 3.1 (Shaw & Dufour 1995). The atomic data adopted are those included in the May 1997 version of *nebular*, except for the update of the S III collisional strengths from Tayal & Gupta (1999). Electron temperatures were obtained from as many lines as possible for 32 H II regions, where at least one auroral line was detected. These temperatures are listed in Table 10, where we prefer to use $T(7325)$ instead of T[O II], and similarly for the other lines, to indicate the possibility that these temperatures might be different from the real ionic temperatures. The [O II] λ7325 line is usually the strongest auroral line in the measured spectra, and was detected for all H II regions included in Table 10. On the other hand, [S II] λ4072, from which $T(4072)$ was derived, has been seldom detected, its measurement made difficult by low signal-to-noise in the spectra. Both $T(5755)$ and $T(6312)$ were computed for about half of the sample in Table 10.

The empirical relationship found between the various temperatures is displayed in Fig. 16. In the top panel we plot $T(5755)$ against $T(6312)$. Garnett (1992) gave simple equations relating electron temperatures from different ions, based on a 3-zone temperature stratification of H II regions. The temperatures T[O II], T[N II] and T[S II] are equivalent to the electron temperature in the low-excitation zone, while T[O III] represents the temperature in the high-excitation zone. An intermediate-excitation zone is measured by T[S III]. The equations published by Garnett (1992), based on photoionization models by Stasińska (1982), are commonly used whenever the data do not allow the determination of the electron temperature in each excitation zone:

$$T[\mathrm{S\,III}] = 0.83\,T[\mathrm{O\,III}] + 1700\ \mathrm{K}, \quad (1)$$

$$T[\mathrm{N\,II}] = T[\mathrm{O\,II}] = 0.70\,T[\mathrm{O\,III}] + 3000\ \mathrm{K}. \quad (2)$$

Naturally, an empirical verification of these, or equivalent, equations is highly valuable for extragalactic abundance studies. Recently Bresolin et al. (2004), in their study of metal-rich H II regions in the galaxy M 51, showed that the predicted T[S III] – T[N II] relation is in good agreement with the experimental data. The top panel of Fig. 16 shows that good agreement with the model predictions:

$$T[\mathrm{S\,III}] = 1.19\,T[\mathrm{O\,II}] - 1857\ \mathrm{K}, \quad (3)$$

(obtained combining Eqs. (1) and (2)), shown here by the dashed line, is also found in the current H II region sample. These results seem to support the validity of these equations, at least in the electron temperature range considered (6000–9000 K). On the other hand, the results of the remaining two comparisons displayed in Fig. 16 is less satisfactory. In the 3-zone representation $T(5755)$, $T(7325)$ and $T(4072)$ should all be representative of the low-excitation zone, and therefore equivalent. However, $T(7325)$ seems to overestimate the temperature if compared to $T(5755)$, while the opposite happens for $T(4072)$. In the case of the [O II] λ7325 line, while it is true that accounting for a recombination component goes in the right direction to alleviate the discrepancy (for example using the empirical formula given by Liu et al. 2000), the effect, when corrected as in Kennicutt et al. (2003), would be negligible in our sample. However, a correct treatment of recombination should take into account the effect of temperature gradients within ionized nebulae, and future work on the importance of the temperature structure of a number of H II regions in our sample will shed some light on this important issue. Regarding $T(4072)$, more observational data need to be collected before confirming the offset suggested by Fig. 16. The reasons for these discrepancies are thus unclear at the moment, but our results remind us that, even though the 3-zone representation might be a useful tool for the interpretation of nebular spectra, it remains a simplification of the excitation and ionization structure of real H II regions.

To conclude this section, before we approach the estimate of the chemical abundances, we must obtain the temperatures required in the 3-zone representation. As a minimum, we need to derive the temperature of the high-excitation zone, since T[O III] cannot be measured from our data. This can be done by means of Eqs. (1) and (2), combining the results with a weighted mean when both $T(6312)$ and $T(5755)$ are available [$T(7325)$ was not considered for this estimate]. These two temperatures also provided T_e estimates for the low- and intermediate-excitation zones, using again Eqs. (1) and (2) when needed. Finally, for those H II regions where only $T(7325)$ was available, we set the low-excitation temperature equal to $T(7325)$, and derived the high- and intermediate-excitation zone temperatures from Eqs. (1) and (2). We have less confidence in the latter estimates than those obtained from the availability of both $T(6312)$ and $T(5755)$, because of the results illustrated in Fig. 16. We report in Table 11 the adopted electron temperatures thus obtained, and used for determining the abundances.

5. Chemical abundance: direct method

The temperatures derived in the previous section can now be used to measure the nebular chemical abundances, keeping in mind, however, the caution expressed at the beginning of Sect. 4 regarding the abundance biases in metal-rich H II regions. With the 3-zone representation we have derived ionic abundances, adopting the electron temperature of the low-excitation zone for O^+, N^+ and S^+, the temperature of the intermediate-excitation zone for S^{+2}, and the temperature of the high-excitation zone for O^{+2} (see Table 11). In order to compute total element abundances, we then made the common assumptions: $O/H = (O^+ + O^{+2})/H^+$, $N/O = N^+/O^+$, while for S/O we have used the ionization correction formula of Stasińska (1978), as used in Bresolin et al. (2004) and Kennicutt et al. (2003). The abundances of oxygen relative to hydrogen and of nitrogen and sulphur relative to oxygen thus derived are reported in Table 12.

The reader should bear in mind that these abundances will be checked against a more detailed analysis, to be presented in a forthcoming paper, to which we postpone the report on the

Table 10. Temperatures measured from auroral lines.

ID	$T(7325)$ (K)	$T(5755)$ (K)	$T(6312)$ (K)	$T(4072)$ (K)
		NGC 1232		
02.....	11 200 ± 1300	...	...	...
04.....	10 800 ± 800	...	10 900 ± 700	10 400 ± 1500
05.....	8600 ± 300	7800 ± 700	7200 ± 400	7200 ± 400
06.....	9400 ± 700	8000 ± 1000	...	...
07.....	7300 ± 400	6400 ± 700	6800 ± 800	...
10.....	7400 ± 600	...	...	...
11.....	16 400 ± 1500	...	...	14 700 ± 2300
14.....	9000 ± 400	8500 ± 400	8339 ± 500	8100 ± 400
15.....	10 900 ± 800	...	...	...
		NGC 1365		
03.....	7800 ± 1000	...	...	...
05.....	7600 ± 400	7000 ± 800	6600 ± 700	6300 ± 500
08.....	8200 ± 600	8200 ± 600	7700 ± 500	...
12.....	7400 ± 600	...	...	...
14.....	6500 ± 400	...	7100 ± 1000	...
15.....	8700 ± 500	8000 ± 300	7500 ± 300	5100 ± 300
16.....	9700 ± 800	...	8200 ± 1100	...
17.....	9500 ± 800	...	...	6000 ± 500
		NGC 2903		
06.....	11 200 ± 800	...	...	...
		NGC 2997		
04.....	10 000 ± 600	...	8000 ± 500	...
05.....	9600 ± 600	7300 ± 700	6700 ± 400	...
06.....	9100 ± 400	7900 ± 500	7700 ± 300	7000 ± 600
07.....	8300 ± 500	7700 ± 600	7200 ± 500	...
11.....	9300 ± 1200	...	...	...
13.....	8700 ± 400	...	5600 ± 400	...
14.....	8800 ± 1200	...	...	...
		NGC 5236		
03.....	8800 ± 500	8100 ± 600	7300 ± 400	...
05.....	<8700 ± 1000	8700 ± 400	...	...
06.....	7500 ± 800	7700 ± 1000	6700 ± 700	...
09.....	8100 ± 700	...	...	...
11.....	8900 ± 400	5900 ± 200	4800 ± 200	...
14.....	7000 ± 600	6600 ± 800	...	...
16.....	9000 ± 400	6900 ± 400	5400 ± 300	...

detailed abundance properties of our H II region sample. In this section we briefly summarize the trends of the S/O and N/O abundance ratios with O/H, in order to characterize our sample and make a comparison with works in the literature. The variation of heavy element ratios, in particular N/O, with metallicity offers a crucial insight into the nucleosynthetic nature of these elements (Henry et al. 2000), and it is therefore important to extend the measurements to metal-rich environments, such as those encountered in the central regions of spiral galaxies (Bresolin et al. 2004; Garnett et al. 2004b).

The S/O and N/O ratios of all objects included in Table 12 are plotted as a function of O/H in Fig. 17, where we add a comparison sample of extragalactic H II regions with published T_e-based abundances, extracted from Garnett et al. (1997, NGC 2403), Kennicutt et al. (2003, M101) and Bresolin et al. (2004, M 51), and shown by the small full square symbols. The objects from our new observations, indicated by the usual symbols (defined in Fig. 8) and the corresponding error bars, are generally consistent with the known trends of roughly constant S/O [$\log(\mathrm{S/O}) \simeq -1.6$] and N/O increasing with O/H in

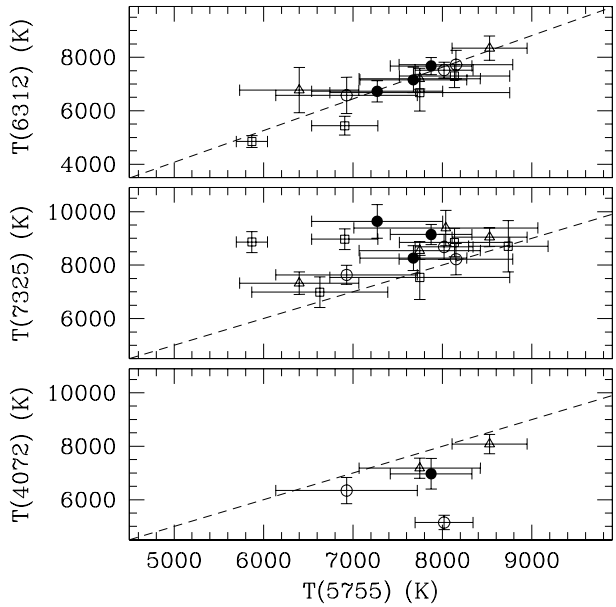

Fig. 16. The temperature $T(5755)$ determined from the [N II] λ5755/[N II] $\lambda\lambda$6548,6583 ratio compared with the temperatures measured from the auroral lines [S III] λ6312 (*top*), [O II] λ7325 (*middle*) and [S II] λ4072 (*bottom*). In the top panel the dashed line represents the relationship predicted by the models of Garnett (1992), while in the remaining 2 panels the line shows the location in the diagrams where $T(5755) = T(7325)$ and $T(5755) = T(4072)$, respectively.

the high-metallicity regime, although a number of outliers are clearly present at the low-abundance end. This is likely due to the inadequacy of the inferred temperatures for the 3-zone representation in those cases where, among the auroral lines, only [O II] λ7325 was measured. In fact, the abundances for the comparison sample of H II regions in NGC 2403, M101 and M 51 were derived from the measurement of [N II] λ5755 and [S III] λ6312 in their spectra, while disregarding abundances based on the [O II] λ7325 auroral line. As shown in Sect. 4, $T(7325)$ appears to overestimate the electron temperature in the low-excitation zone, thus leading to an underestimate of the oxygen abundance. If we limit the diagram to include only those objects in the VLT sample where [N II] λ5755 and/or [S III] λ6312 are available (marked by asterisks in Table 12), which arguably allows a more robust application of the 3-zone model, a picture which is more consistent with the previous abundance works emerges, as seen in Fig. 18. In the bottom panel of this figure we have also drawn as a reference (dashed line) the simple model for N/O introduced by Kennicutt et al. (2003) as the sum of a primary, constant component [$\log(N/O) = -1.5$] and a secondary component, for which N/O is proportional to O/H [$\log(N/O) = \log(O/H) + 2.2$], which reproduces fairly well the metallicity dependence of N/O in the H II regions of M101. The scatter in N/O at constant oxygen abundance is well-known (see Henry et al. 2000), so it is not surprising to find objects deviating (at the 1–2σ level) from the dashed line.

Among the objects included in Table 12, we draw attention to a few interesting cases. First of all, NGC 1232-11,

Table 11. Adopted temperatures for the 3-zone representation.

ID	$T(O^+, N^+, S^+)$ (K)	$T(S^{+2})$ (K)	$T(O^{+2})$ (K)
	NGC 1232		
02.....	11 200 ± 1300	11 400 ± 1500	11 700 ± 1800
04.....	10 700 ± 600	10 900 ± 700	11 100 ± 800
05.....	7700 ± 700	7200 ± 400	6700 ± 400
06.....	8000 ± 1000	7700 ± 1200	7200 ± 1500
07.....	6400 ± 700	6800 ± 800	5500 ± 700
10.....	7400 ± 600	6900 ± 800	6300 ± 900
11.....	16 400 ± 1500	17 600 ± 1800	19 100 ± 2200
14.....	8500 ± 400	8300 ± 500	7900 ± 400
15.....	10 900 ± 800	11 100 ± 1000	11 300 ± 1200
	NGC 1365		
03.....	7800 ± 1000	7400 ± 1200	6800 ± 1400
05.....	6900 ± 800	6600 ± 700	5800 ± 600
08.....	8200 ± 600	7700 ± 500	7300 ± 500
12.....	7400 ± 600	6900 ± 700	6200 ± 800
14.....	7500 ± 900	7100 ± 1000	6500 ± 1100
15.....	8000 ± 300	7500 ± 300	7100 ± 200
16.....	8500 ± 1000	8300 ± 1100	7900 ± 1200
17.....	9500 ± 800	9400 ± 900	9300 ± 1100
	NGC 2903		
06.....	11 200 ± 800	11 500 ± 1000	11 800 ± 1200
	NGC 2997		
04.....	8300 ± 500	8000 ± 500	7600 ± 600
05.....	7300 ± 700	6700 ± 400	6100 ± 400
06.....	7900 ± 500	7700 ± 300	7100 ± 300
07.....	7700 ± 600	7200 ± 500	6600 ± 400
11.....	9300 ± 1200	9200 ± 1400	9000 ± 1700
13.....	6300 ± 400	5600 ± 400	4700 ± 500
14.....	8800 ± 1200	8600 ± 1400	8300 ± 1700
	NGC 5236		
03.....	8100 ± 600	7300 ± 400	7000 ± 400
05.....	8700 ± 400	8500 ± 500	8200 ± 500
06.....	7700 ± 1000	6700 ± 700	6300 ± 700
09.....	8100 ± 700	7800 ± 800	7300 ± 900
11.....	5900 ± 200	4800 ± 200	4000 ± 200
14.....	6600 ± 800	6000 ± 900	5200 ± 900
16.....	6900 ± 400	5400 ± 400	5000 ± 300

which is characterized by peculiar emission line ratios (e.g. large [O I] λ6300/Hβ) and which appears to deviate from the H II region sequence in Fig. 11, has also a much higher T_e than the rest of the sample, and a correspondingly small O/H for its inner position in the galaxy. The wavelengths of its emission lines are not discordant with those of the remaining H II regions in NGC 1232, therefore it is not a background emission-line galaxy at larger redshift.

The oxygen abundance derived for NGC 1232-07, $12 + \log(O/H) = 8.9 \pm 0.3$, is in good agreement with the value of 8.95 ± 0.20 reported by Castellanos et al. (2002, their object CDT1). At the time of their publication, this object was the most metal-rich extragalactic H II region with an electron temperature measured from auroral lines. In our VLT sample,

Table 12. Abundance estimates from the 3-zone representation.

ID	12 + log (O/H)	log (N/O)	log (S/O)
	NGC 1232		
02	8.07 ± 0.19	−1.11 ± 0.34	−1.48 ± 0.27
04 *	8.20 ± 0.09	−1.20 ± 0.14	−1.73 ± 0.11
05 *	8.72 ± 0.17	−0.99 ± 0.36	−1.68 ± 0.22
06 *	8.47 ± 0.32	−0.84 ± 0.60	−1.89 ± 0.51
07 *	8.90 ± 0.31	−0.84 ± 0.58	−1.82 ± 0.49
10	8.44 ± 0.22	−0.69 ± 0.37	−1.51 ± 0.31
11	7.43 ± 0.12	−0.29 ± 0.18	−1.06 ± 0.15
14 *	8.50 ± 0.10	−0.93 ± 0.15	−1.65 ± 0.12
15	8.16 ± 0.13	−1.12 ± 0.20	−1.61 ± 0.16
	NGC 1365		
03	8.62 ± 0.33	−0.94 ± 0.61	−1.56 ± 0.54
05 *	8.71 ± 0.31	−0.84 ± 0.60	−1.67 ± 0.47
08 *	8.38 ± 0.15	−0.74 ± 0.28	−1.52 ± 0.20
12	8.57 ± 0.20	−0.77 ± 0.33	−1.61 ± 0.28
14 *	8.58 ± 0.29	−0.86 ± 0.55	−1.67 ± 0.46
15 *	8.54 ± 0.08	−0.71 ± 0.13	−1.47 ± 0.09
16 *	8.44 ± 0.25	−0.97 ± 0.49	−1.66 ± 0.38
17	8.33 ± 0.16	−0.93 ± 0.27	−1.57 ± 0.21
	NGC 2903		
06	7.70 ± 0.13	−0.41 ± 0.19	−1.01 ± 0.16
	NGC 2997		
04 *	8.71 ± 0.12	−1.25 ± 0.20	−1.75 ± 0.15
05 *	8.82 ± 0.22	−0.97 ± 0.48	−1.68 ± 0.30
06 *	8.57 ± 0.11	−0.90 ± 0.20	−1.58 ± 0.14
07 *	8.56 ± 0.17	−0.81 ± 0.31	−1.54 ± 0.23
11	8.04 ± 0.26	−0.54 ± 0.48	−1.24 ± 0.39
13 *	8.92 ± 0.19	−0.81 ± 0.30	−1.57 ± 0.27
14	8.17 ± 0.30	−0.64 ± 0.58	−1.30 ± 0.48
	NGC 5236		
03 *	8.59 ± 0.13	−0.78 ± 0.28	−1.59 ± 0.17
05[a]	7.78 ± 0.10	−0.22 ± 0.16	−1.10 ± 0.12
06 *	8.32 ± 0.30	−0.49 ± 0.64	−1.24 ± 0.46
09	7.76 ± 0.19	−0.16 ± 0.30	−1.08 ± 0.26
11 *	8.94 ± 0.09	−0.39 ± 0.13	−1.23 ± 0.12
14 *	8.48 ± 0.34	−0.49 ± 0.64	−1.43 ± 0.56
16 *	8.78 ± 0.12	−0.68 ± 0.22	−1.29 ± 0.18

NOTES: for the objects marked by an asterisk the abundances have been derived from the measurement of either [N II] λ5755, [S III] λ6312, or both.
[a] O/H is a lower limit, N/O and S/O are upper limits (see note in Table 9).

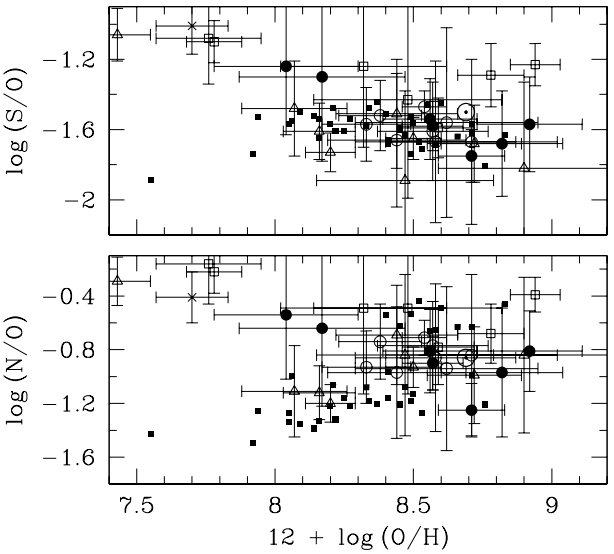

Fig. 17. The S/O (*top*) and N/O (*bottom*) abundance ratio trends with O/H for all objects in Table 12. A comparison sample, drawn from Garnett et al. (1997, NGC 2403), Kennicutt et al. (2003, M 101) and Bresolin et al. (2004, M 51), is shown by small full square symbols. The solar values, indicated by the ⊙ symbol, are taken from Lodders (2003).

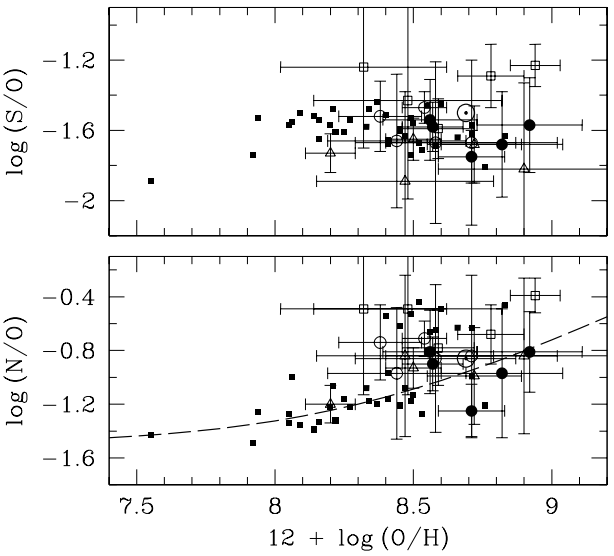

Fig. 18. Same as Fig. 17, but including only nebulae from the VLT sample where the electron temperature has been computed from the availability of at least one of the [N II] λ5755 and [S III] λ6312 auroral lines (objects marked by asterisks in Table 12). The dashed line represents a simple model, in which a primary nitrogen component is superposed on a secondary component, which is proportional to O/H.

the most metal-rich nebulae do not exceed the oxygen abundance of this H II region. In particular, for NGC 5236-11, in the very nucleus of the M 83 galaxy, we find an abundance $12 + \log(\mathrm{O/H}) = 8.94 \pm 0.09$, while for NGC 2997-13 we find $12 + \log(\mathrm{O/H}) = 8.92 \pm 0.19$. Therefore, with the direct method adopted in this work, applied to observations obtained at the VLT, we have not been able to find abundances larger than about 1.6 times the solar one [$12 + \log(\mathrm{O/H})_\odot = 8.69$]. This conclusion, however, is likely to be revised (in either direction) if biases due to temperature stratification (Stasińska 2005) are duely taken into account.

To conclude this preliminary look at the abundance properties of our sample, we plot in Fig. 19 the indicator R_{23} as a function of the T_e-based oxygen abundance, again including only objects with [N II] λ5755 and/or [S III] λ6312 detections. In this diagram we also show the points corresponding to the H II regions in NGC 2403, M 101 and M 51 from the papers mentioned above (small full square symbols). The two widely used $R23$ calibrations of Edmunds & Pagel (1984) and Pilyugin (2001) (the latter applicable for

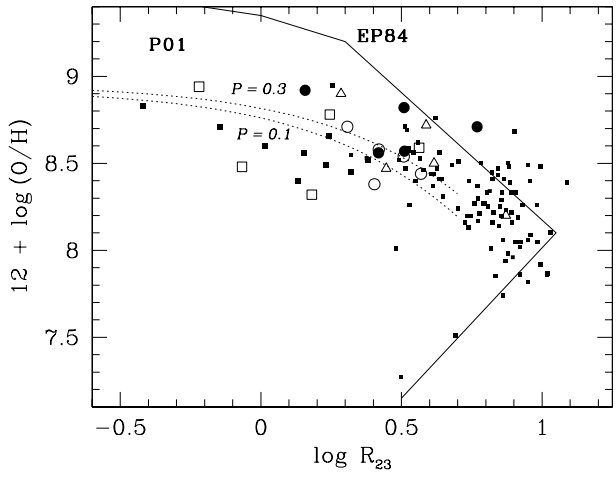

Fig. 19. The abundance indicator R_{23} as a function of oxygen abundance, including all H II regions with measured [N II] λ5755 or [S III] λ6312 auroral lines. The comparison sample (small squares) is the same as in Fig. 17. The continuous and dotted lines show, respectively, the R_{23} calibrations by Edmunds & Pagel (1984) (EP84) and Pilyugin (2001) (P01). The latter has been drawn for two different values of the excitation parameter, $P = 0.1$ and $P = 0.3$. This range encompasses the majority of the H II regions in the VLT sample.

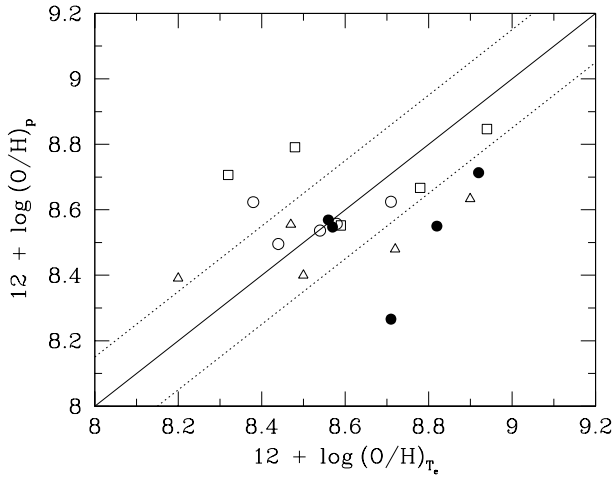

Fig. 20. Comparison between direct (T_e-based) abundances and those estimated via the R_{23} calibration of Pilyugin (2001). The dotted lines are drawn 0.15 dex below and above the line of equal value.

$12 + \log(\mathrm{O/H}) > 8.2$, according to the latter author) are shown by the continuous and dotted lines, respectively. The Pilyugin (2001) calibration attempts to account for the sensitivity of R_{23} to the ionization parameter, by introducing the quantity $P = [\mathrm{O\,III}]\,\lambda\lambda 4959{,}5007/([\mathrm{O\,II}]\,\lambda 3727 + [\mathrm{O\,III}]\,\lambda\lambda 4959{,}5007)$. Two curves, corresponding to $P = 0.1$ and $P = 0.3$, the same values used in Fig. 13 to bracket most of the H II regions in the current sample, are drawn in Fig. 19. As can be seen, the most metal-rich H II regions, in particular those in NGC 5236 (open squares), reach values of R_{23} that are comparable to those found in M 51 H II regions by Bresolin et al. (2004), and have similar O/H abundances. Fig. 19 confirms earlier findings (Pindao et al. 2002; Kennicutt et al. 2003; Bresolin et al. 2004) that indicated how some of the calibrations of statistical methods available in the literature (e.g. Edmunds & Pagel 1984; Zaritsky et al. 1994) can severely overestimate the abundance of metal-rich H II regions, while others (e.g. Pilyugin 2001) might be less affected by systematic differences compared to direct abundances, even though the two methods can still give significantly discrepant results for individual H II regions. This is shown in Fig. 20, where we compare the T_e-based abundances with those estimated from the Pilyugin (2001) R_{23} calibration. The dotted lines are drawn 0.15 dex above and below the line of equal value (full line), to aid in the comparison with a similar diagram presented by Pilyugin et al. (2004, their Fig. 15). For our metal-rich sample we clearly find a larger scatter than found by these authors.

6. Conclusions

We have presented new optical VLT spectroscopy for a sample of extragalactic H II regions, comprising about 70 nebulae, distributed in five galaxies: NGC 1232, NGC 1365, NGC 2903, NGC 2997 and NGC 5236. The target galaxies were selected in order to maximize the odds of obtaining spectra of truly metal-rich H II regions, with oxygen abundances around the solar value and above. Our principal goal in this first paper of a series was to present the emission line measurements, in particular for the 32 objects where we have been able to detect auroral lines for different ions. With the aid of these lines, and adopting a 3-zone description for the excitation structure of the nebulae, we have derived electron temperatures and abundances of O, N and S, neglecting the abundance biases that are likely to be introduced by the temperature stratification of the nebulae. The impact of these biases on the chemical abundance measurements presented here will be assessed in a future publication.

The direct (T_e-based) method of abundance determination has provided only a handful of objects of genuine high metallicity, that is well above solar, up to $12 + \log(\mathrm{O/H}) \simeq 8.9$. We have measured a direct abundance for two additional H II regions, besides the CDT1 nebula studied by Castellanos et al. (2002), where the oxygen abundance reaches this value: our NGC 2997-13 and NGC 5236-11. Of course, this result does not exclude the presence of H II regions of higher metallicity in these galaxies, but it is interesting to note that one of these objects, NGC 5236-11, lies at the center, i.e. where we expect the oxygen abundance to be highest, of M 83, a galaxy which has been known to be among the most metal-rich spirals for a long time. The T_e-based oxygen abundance of an H II region near the center of M 51, another metal-rich spiral galaxy, was found by Bresolin et al. (2004) to exceed by only 40% the solar oxygen abundance. It thus appears conceivable that we have started to measure electron temperatures among the most metal-rich H II regions in spiral galaxies. Deep spectroscopy of a larger number of H II regions within the same galaxies studied here might provide better constraints on the metallicity at the top-end of the scale.

What appears to be well established is that at high metallicity the direct abundances are systematically smaller than the abundances derived from most statistical methods calibrated by means of photoionization models. We confirm earlier results

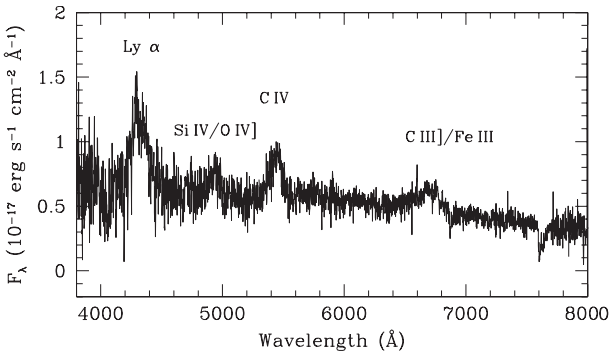

Fig. A.1. The spectrum of a QSO from our MOS setup in NGC 1365.

that provided some of the first solid empirical evidence for this discrepancy (Kennicutt et al. 2003, Garnett et al. 2004a, Bresolin et al. 2004). With the availability of the new direct measurements provided in these works, some of the existing calibrations for statistical methods appear inconsistent with the direct measurements at high metallicity. A thorough analysis of abundance calibrators taking into account strong electron temperature stratification at high metallicities and additional observational data (e.g. from infrared fine structure lines) is however needed. The widespread use of strong line indicators in estimating the chemical abundances of star-forming regions both at low and high redshift makes this an obviously important issue.

Appendix A: Serendipitous discovery of a $z \simeq 2.55$ QSO

The spectrum of our target object for slitlet 2 in the NGC 1365 MOS setup is that of a QSO, instead of a star-forming region within this galaxy. The position relative to the galaxy center is (−26″, 182″), corresponding to RA = $03^h\ 33^m\ 34\overset{s}{.}2$, Dec = −36° 05′ 23″.8. This object is marked by the open circle at the top of Fig. 2. By convolving the flux-calibrated spectrum with the response function of broad-band filters in the Johnson photometric system, we have derived $V = 21.9$ and $B-V = 0.4$. The broad lines detected in the spectrum (see Fig. A.1) have been used to derive a redshift $z \simeq 2.55$.

References

Allende Prieto, C., Lambert, D. L., & Asplund, M. 2001, ApJ, 556, L63
Alloin, D., Collin-Soufrin, S., Joly, M., & Vigroux, L. 1979, A&A, 78, 200
Alloin, D., Edmunds, M. G., Lindblad, P. O., & Pagel, B. E. J. 1981, A&A, 101, 377
Bresolin, F., & Kennicutt, R. C. 2002, ApJ, 572, 838
Bresolin, F., Kennicutt, R. C., & Garnett, D. R. 1999, ApJ, 510, 104
Bresolin, F., Garnett, D. R., & Kennicutt, R. C. 2004, ApJ, 615, 228
Cardelli, J. A., Clayton, G. C., & Mathis, J. S. 1989, ApJ, 345, 245
Castellanos, M., Díaz, A. I., & Terlevich, E. 2002, MNRAS, 329, 315
Crowther, P. A., Hadfield, L. J., Schild, H., & Schmutz, W. 2004, A&A, 419, L17
de Naray, R. K., McGaugh, S. S., & de Blok, W. J. G. 2004, MNRAS, 355, 887
Denicoló, G., Terlevich, R., & Terlevich, E. 2002, MNRAS, 330, 69
Díaz, A. I., & Pérez-Montero, E. 2000, MNRAS, 312, 130
Dopita, M. A., Kewley, L. J., Heisler, C. A., & Sutherland, R. S. 2000, ApJ, 542, 224
Dopita, M. A., & Evans, I. N. 1986, ApJ, 307, 431
Edmunds, M. G., & Pagel, B. E. J. 1984, MNRAS, 211, 507
Freedman, W. L., Madore, B. F., Gibson, B. K., et al. 2001, ApJ, 553, 47
Garnett, D. R. 1992, AJ, 103, 1330
Garnett, D. R., Shields, G. A., Skillman, E. D., Sagan, S. P., & Dufour, R. J. 1997, ApJ, 489, 63
Garnett, D. R., Kennicutt, R. C., & Bresolin, F. 2004a, ApJ, 607, L21
Garnett, D. R., Edmunds, M. G., Henry, R. B. C., Pagel, B. E. J., & Skillman, E. D. 2004b, AJ, 128, 2772
Goldader, J. D., Joseph, R. D., Doyon, R., & Sanders, D.B. 1997, ApJ, 474, 104
González Delgado, R. M., Leitherer, C., Stasińska, G., & Heckman, T. M. 2002, ApJ, 580, 824
Henry, R. B. C., Edmunds, M. G., & Köppen, J. 2000, ApJ, 541, 660
Howarth. I. D. 1983, MNRAS, 203, 301
Hummer, D. G., & Storey, P. J. 1987, MNRAS, 244, 801
Kennicutt, R. C., Bresolin, F., French, H., & Martin, P. 2000, ApJ, 537, 589
Kennicutt, R. C., Bresolin, F., & Garnett, D. R. 2003, ApJ, 591, 801
Kobulnicky, H. A., & Kewley, L. J. 2004, ApJ, 617
Kobulnicky, H. A., Kennicutt, R. C., & Pizagno, J. L. 1999, ApJ, 514, 544
Liu, X.-W., Storey, P. J., Barlow, M. J., et al. 2000, MNRAS, 312, 585
Lodders, K. 2003, ApJ, 591, 1220
McCall, M. L., Rybski, P. M., & Shields, G. A. 1985, ApJS, 57, 1
McGaugh, S. S. 1991, ApJ, 380, 140
Meynet, G. 1995, A&A, 298, 767
Pagel, B. E. J., Edmunds, M. G., Blackwell, D. E., Chun, M. S., & Smith, G. 1979, MNRAS, 189, 95
Pettini, M., & Pagel, B. E. J. 2004, MNRAS, 348, 59
Pilyugin, L. S. 2001, A&A, 369, 594
Pilyugin, L. S., Vílchez, J. M., & Contini, T., 2004, A&A, 425, 849
Pindao, M., Schaerer, D., González Delgado, R. M., & Stasińska, G. 2002, A&A, 394, 443
Roy, J.-R., & Walsh, J. R. 1997, MNRAS, 288, 715
Roy, J.-R., & Walsh, J. R. 1988, MNRAS, 234, 977
Schaerer, D., & Vacca, W. D. 1998, ApJ, 497, 618
Schaerer, D., Guseva, N. G., Izotov, Y. I., & Thuan, T. X. 2000, A&A, 362, 53
Seaton, M. J. 1979, MNRAS, 187, 73
Shapley, A. E., Erb, D. K., Pettini, M., Steidel, C. C., & Adelberger, K. L. 2004, ApJ, 612, 108
Shaw, R. A., & Dufour, R. J. 1995, PASP, 107, 896
Stasińska, G. 1978, A&A, 66, 257
Stasińska, G. 1982, A&AS, 48, 299
Stasińska, G. 2005, A&A, 434, 507
Tayal, S. S., & Gupta, G. P. 1999, ApJ, 526, 544
Thim, F., Tammann, G. A., Saha, A., et al. 2003, ApJ, 590, 256
Thornley, M. D., Forster Schreiber, N. M., Lutz, D., et al. 2000, ApJ, 539, 641
van Zee, L., Salzer, J. J., Haynes, M. P., O'Donoghue, A. A., & Balonek, T. J. 1998, AJ, 116, 2805
Vila-Costas, M. B., & Edmunds, M. G. 1992, MNRAS, 259, 121
Walsh, J. R., & Roy, J.-R. 1989, ApJ, 341, 722
Zaritsky, D., Kennicutt, R. C., & Huchra, J. P. 1994, ApJ, 420, 87